

Article

Assessing Multi-Scale Atmospheric Circulation Patterns for Improvements in Sub-Seasonal Precipitation Predictability in the Northern Great Plains

Carlos M. Carrillo ¹  and Francisco Muñoz-Arriola ^{1,2,*} 

¹ Hydroinformatics and Integrated Hydroclimate Research Lab, Institute of Agriculture and Natural Resources, Department of Biological Systems Engineering, University of Nebraska-Lincoln, Lincoln, NE 68583, USA; carloscc@email.arizona.edu

² Climate Analytics, Analysis, and Synthesis for Action Research Collective, Institute of Agriculture and Natural Resources, School of Natural Resources, University of Nebraska-Lincoln, Lincoln, NE 68583, USA

* Correspondence: fmunoz@unl.edu; Tel.: +1-402-472-0850

Abstract: This study leverages the relationships between the Great Plains low-level jet (GP-LLJ) and the circumglobal teleconnection (CGT) to assess the enhancement of 30-day rainfall forecast in the Northern Great Plains (NGP). The assessment of 30-day simulated precipitation using the Climate Forecast System (CFS) is contrasted with the North American Regional Reanalysis, searching for sources of precipitation predictability associated with extended wet and drought events. We analyze the 30-day sources of precipitation predictability using (1) the characterization of dominant statistical modes of variability of 900 mb winds associated with the GP-LLJ, (2) the large-scale atmospheric patterns based on 200 mb geopotential height (HGT), and (3) the use of GP-LLJ and CGT conditional probability distributions using a continuous correlation threshold approach to identify when and where the forecast of NGP precipitation occurs. Two factors contributing to the predictability of precipitation in the NGP are documented. We found that the association between GP-LLJ and CGT occurs at two different scales—the interdiurnal and the sub-seasonal, respectively. The CFS reforecast suggests that the ability to forecast sub-seasonal precipitation improves in response to the enhanced simulation of the GP-LLJ and CGT. Using these modes of climate variability could improve predictive frameworks for water resources management, governance, and water supply for agriculture.

Keywords: drought; extended rainfall; sub-seasonal predictability; low-level jet; circumglobal teleconnection; EOF; CFS; NARR



Citation: Carrillo, C.M.; Muñoz-Arriola, F. Assessing Multi-Scale Atmospheric Circulation Patterns for Improvements in Sub-Seasonal Precipitation Predictability in the Northern Great Plains. *Atmosphere* **2024**, *15*, 858. <https://doi.org/10.3390/atmos15070858>

Academic Editor: Anthony R. Lupo

Received: 10 June 2024

Revised: 13 July 2024

Accepted: 17 July 2024

Published: 20 July 2024



Copyright: © 2024 by the authors. Licensee MDPI, Basel, Switzerland. This article is an open access article distributed under the terms and conditions of the Creative Commons Attribution (CC BY) license (<https://creativecommons.org/licenses/by/4.0/>).

1. Introduction

Six major U.S. climate model development institutions (NOAA GFDL, NCAR, NASA GISS, DOE ACME, NASA GMAO, and NCEP CFS—list of acronyms in Table S1) have coordinated efforts to better understand the sources of climate predictability for more than a decade [1]. The motivation behind these modeling efforts is to improve operational sub-seasonal forecasts (30- and 60-day) [2]; however, climate predictability at such temporal lead times is still a major challenge [3–7]. Of particular interest is the sub-seasonal forecasting skill and predictability of precipitation in the United States Northern Great Plains (NGP) during late spring and early summer, May through July [8]. During this season, extended precipitation events, or their absence, may lead to natural disasters, such as the 1993 flood in the Midwest or the 1988 and 2012 droughts (Figures 1 and 2), which are considered some of the costliest events in the history of the United States, with estimated damages of USD 20 and 40 billion, respectively [9,10]. Losses in the NGP included drops in corn yields of about 30% for Nebraska, Iowa, Minnesota, and Illinois, which affected local farming and regional economies [11]. These states lie in the U.S. Midwest, where the corn economy is valued at about USD 50 billion [12]. This region is also considered a production hub for corn,

soybean, cattle, and halves in the United States [13,14], making climate diagnostics and prognostics crucial to food and bio-fuel production and water resources security [15–22].

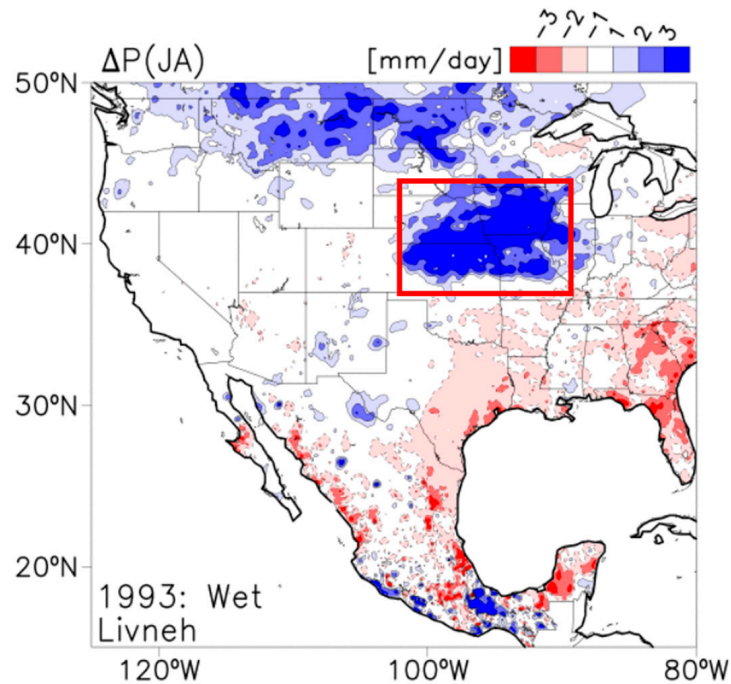


Figure 1. Summer precipitation anomaly (ΔP) of the 1993 July–August (JA) season. Precipitation units are in mm/day and the climatology is used from the 1950–2013 period. The dataset is from [23], and the box defines a region (37.5° – 45° N; 103° – 90° W) for a precipitation index used in the next figures.

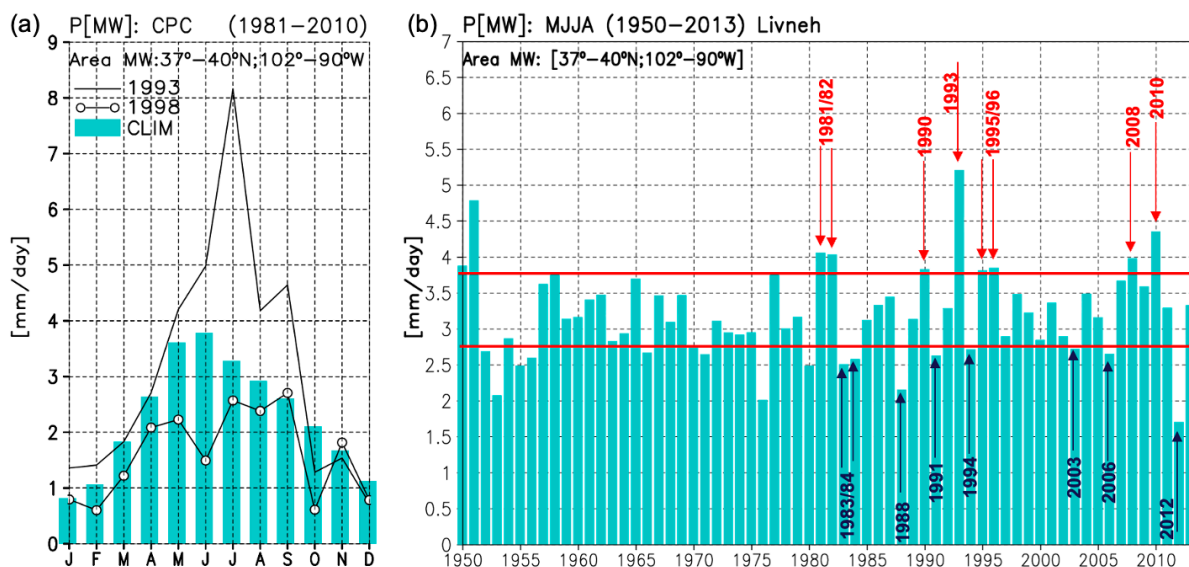


Figure 2. (a) Precipitation climatology (P) in bars for the Northern Great Plains–Midwest region ($MW = 37.5^{\circ}$ – 45° N; 103° – 90° W). The precipitation associated with the 1993 flood and 1988 drought is shown as a black line to illustrate the monthly changes compared to the 1981–2010 climatology. (b) Interannual variability of late spring–early summer (May through August) precipitation over the Northern Great Plains–Midwest region (37.5 – 45° N; 103 – 90° W). The 1993 historical flood event is highlighted, as well as other major wet (red arrows) and dry (blue arrows) years since 1950. The dataset is from [23].

Precipitation variability in the NGP has been related to the spatial and temporal variability of the Great Plains low-level jet (GP-LLJ) [24–26]. The GP-LLJ is the maximum wind frequency in the west region of Oklahoma–Kansas. During summer, NGP precipitation and the GP-LLJ are linked through the transport of moisture from the Gulf of Mexico, the region’s primary source of moisture. The GP-LLJ can be identified using wind data from rawinsonde stations [24] and wind profiler observations [26]. Wind at 900 mb is in several retrospective reanalyses [27], such as NCEP-NCAR [28] and the North American Regional Reanalysis (NARR) [29]. The GP-LLJ, which has its maximum annual cycle during May through July (with a peak in July), facilitates efficient moisture transport through an extensive plains surface center at 900 mb and along 95° W [27].

Rainfall variability of the Northern Great Plains is also linked to large-scale atmospheric teleconnections [27,30,31]. At 200 mb, the association between the GP-LLJ index and geopotential height (HGT) shows a positive strength center over Tennessee, acting over the country’s eastern half, and a Rossby-wave train pattern [32]. This geopotential height pattern matches the interannual variability characteristic of the atmospheric circumglobal teleconnection (CGT) [33]. Observation and modeling indicate that CGT affects summer precipitation in the United States [30,31]. The CGT pattern with one center of action located over North America is essential in driving the variability of summer precipitation over the Northern Hemisphere [33]. The authors [30] showed that the CGT pattern affects the rainfall distribution during the summer. This evidence can be a source of predictability for precipitation in North America and East Asia. Further, [31] found two CGT climatic modes that affect North America’s summer precipitation in the Southern and the Northern Great Plains. The pattern in the Northern Great Plains is responsible for 16% of the early summer (June–July) variability, as evidenced by the application of empirical orthogonal function (EOF) analyses [30]. These authors showed that the maximum strengthening of the CGT during July matches the maximum transport of low-level moist air from the Gulf of Mexico into the Great Plains. How these two components of U.S. climate variability (the CGT and the low-level jets) affect the predictability of summer precipitation over the NGP region is of significant interest to this study.

Although NGP precipitation variability has been extensively studied for several decades [24,26,27], the predictability in the sub-seasonal range is still a challenge [34,35]. The authors [36] reported that the Climate Forecast System’s (CFS) rainfall forecasting skill is limited at ranges beyond the two-week lead time. An improved initial state in the tropical atmosphere CFS version 2 concerning its predecessor version 1 has been translated into significant improvements in the 15-day range precipitation forecast. A multi-model ensemble prediction seems promising, at least for some variables, such as sea surface temperature [3,36]. Still, comparisons among several models from major national modeling centers and CFS reveal a similar skill for precipitation [36]. Further understanding of the regional-to-global modes of variability, such as the GP-LLJ and CGT and their interaction, can help improve sub-seasonal forecasts, especially in agricultural landscapes reliant on precipitation forecasts for crops.

The following questions arise: How strong is the link between the GP-LLJ and CGT in a modeling framework concerning the evolution of summer precipitation over the Northern Great Plains? Furthermore, how does precipitation predictability vary when the internal dynamics of a GCM capture these two modes of climate variability? In other words, can the interaction between the GP-LLJ and CGT influence precipitation predictability within a prognostic 30-day range? We hypothesize that the forecast skill of precipitation over the NGP can be better assessed if GP-LLJ and CGT’s patterns of variability at the daily to sub-seasonal and daily scales are adequately simulated by the model used. We consider that the GP-LLJ’s regional scale and the CGT’s large-scale circulation could reveal the underlying mechanisms responsible for improving sub-seasonal predictability in the NGP. The objectives are threefold, as follows: (1) estimate the GP-LLJ and CGT indices based on NARR and CFS diagnostic and CFS forecast products for at least 30 years; (2) estimate the correlation threshold to assess the unconditional and conditional causality between NGP

precipitation and the GP-LLJ and CGT indices; and (3) evaluate the 30-day forecast skill of the CFS-based daily precipitation forecast products for NARR data using the conditional association between NGP precipitation and the GP-LLJ and CGT indices. We selected the 30-day length based on the CFS's reported limited 20-day forecast skill [36] and NOAA's Climate Prediction Center efforts to provide 30-day precipitation outlooks [2]. Then, the performance of CFS-based precipitation forecasts was evaluated with the GP-LLJ and CGT simulation for the extended wet and drought events of 1993 and 1988, respectively.

The paper's organization is as follows: Section 2 describes the sources of data, and Section 3 describes the methodology, which explains the estimation of GP-LLJ and CGT indices, correlation thresholds, and associations between precipitation estimates and the forecast products. Section 4 analyzes the results, and Section 5 discusses the paper's central thesis.

2. Materials and Methods

2.1. Data

The following three data sources were selected to capture the observed, simulated, and forecasted atmospheric conditions: gridded precipitation, reanalysis, and retrospective forecasting from CFS.

2.1.1. Observed Gridded Precipitation Products

Daily precipitation values from two datasets were used for climate diagnostics and CFS's ability to simulate the sub-seasonal variability and predictability over the Northern Great Plains region. (1) The gridded gridded precipitation at $1/16^\circ$ spatial resolution [23] was derived from approximately 20,000 NOAA Cooperative observed stations, gridded using the synergraphic mapping system method [37], and scaled monthly to match the long-term mean from the parameter-elevation regressions on independent slopes model (PRISM) [38]. (2) The Climate Prediction Center (CPC) unified gauge-based analysis precipitation data [39] were also used to compare results to a modeling simulation with coarser resolution [40]. CPC-unified precipitation, in its native $0.25^\circ \times 0.25^\circ$ resolution, covers the conterminous United States. Both precipitation datasets have daily resolution and cover the NGP.

2.1.2. NARR Reanalysis

The NARR was used to validate the forecasts. We used the meridional wind at 900 mb (V900) to compute the GP-LLJ index, and HGT at 200 mb was used to calculate the CGT index (see below). The NARR integrates the assimilation of observed hourly precipitation [29], which becomes crucial at daily and sub-seasonal scales to identify the GP-LLJ and its atmospheric response at 200 mb geopotential height.

2.1.3. CFS

The retrospective and forecast CFS connected observations to modeling diagnostics and prognostics. The model skill assessment under known boundary conditions used the same variables from the global CFS retrospective reanalysis (CFS-RR) [41]. The CFS reforecast (CFS-R) skill assessment used fields similar to the CFS-RR dataset. We computed forecasts of 30-day precipitation from the CFS reforecast [36] obtained from the National Centers for Environmental Prediction (NCEP) in its reforecast version. The CFS reforecast was from the NOAA National Operational Model Archive and Distribution System (NOMADS) [42]. The 9-month CFS-R simulations were used on the existing period from 1982 through 2009. For all cases presented here, we took the 12Z initialization from 1 May through 1 September each year. We applied a similar analysis for CFS in forecast mode to assess the predictability skill. The approach explored whether the model using the same reanalysis as initial conditions shows an adequate representation of 30-day precipitation of the NGP associated with the dominant statistical modes of GP-LLJ variability.

2.2. Methodology

The GP-LLJ and CGT patterns of variability were obtained using EOF analyses on 900 mb meridional wind and 200 mb HGT, respectively. The correlations between precipitation and the GP-LLJ and CGT used the historical precipitation distribution and the meridional wind’s temporal PC and the HGT fields, respectively (as observed in Figure 3).

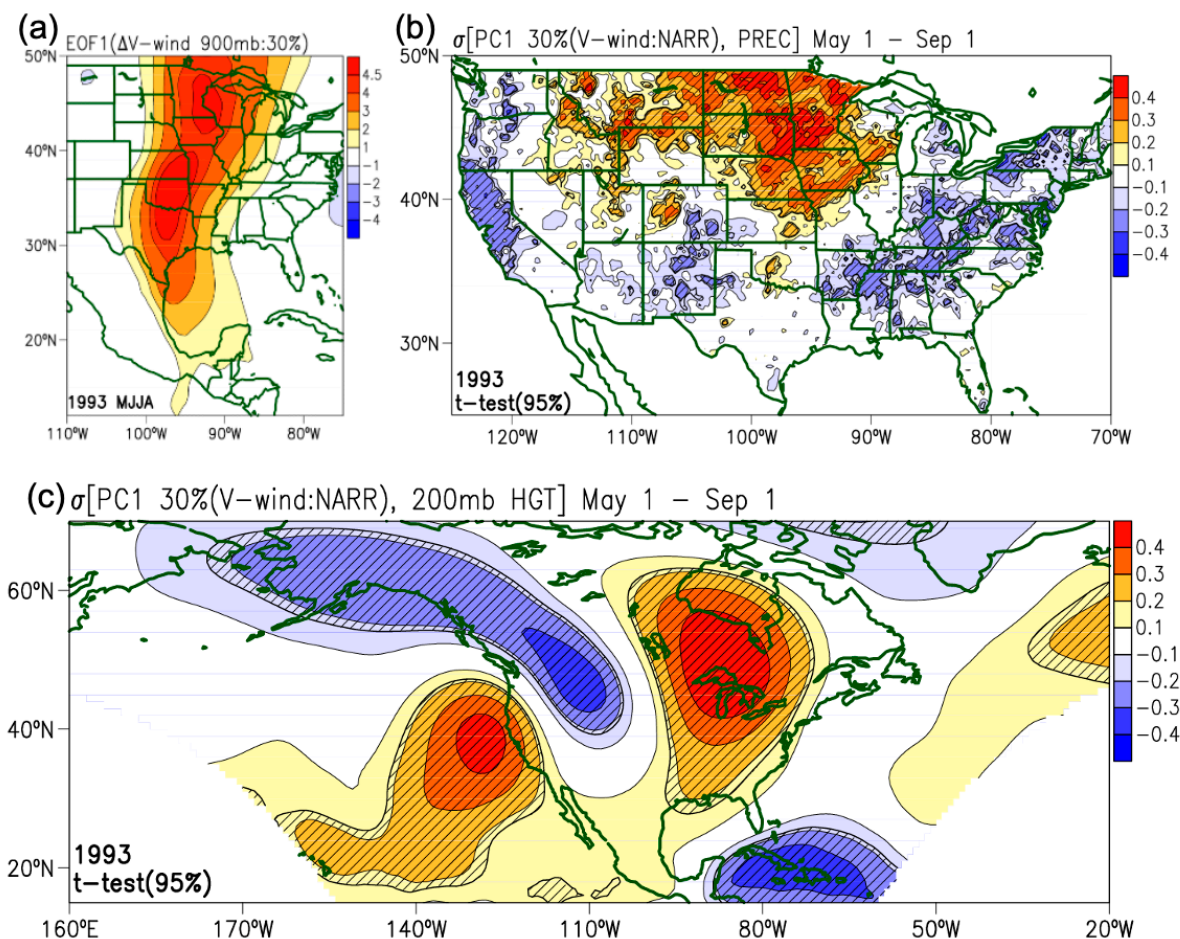


Figure 3. (a) Spatial empirical orthogonal function (EOF1) pattern of 900 mb meridional wind from the North American Regional Reanalysis (NARR) obtained from daily fields from 1 May through 1 September 1993, with an explained variance of 30%. (b) Spatial correlation patterns among the temporal principal component (PC1; from the top figure) and both daily precipitation and (c) daily 200 mb geopotential height (HGT). Oblique lines represent significant values at the t-test 95% level of confidence.

2.2.1. The GP-LLJ Index

Before assessing the predictability skill of the modeling products in forecast mode, we evaluated whether the CFS model using boundary conditions from the reanalysis version (CFS-RR) adequately represented the dominant statistical modes of GP-LLJ variability associated with NGP precipitation. We defined the GP-LLJ temporal index as the temporal principal component (PC) from 900 mb meridional wind during the summer MJJA. We defined the spatial patterns as EOFs and the temporal patterns (or time series) as PCs [43]. The GP-LLJ is usually defined as the maximum wind frequency in a 95° to 100° west region on the Oklahoma–Kansas border at 37° N [24]. We followed a similar EOF approach described in [27,32], using the 900 mb meridional wind anomaly (ΔV) to assess the intraseasonal and interannual variability GP-LLJ. We applied the GP-LLJ EOF analysis over anomalies $\Delta V = V - \bar{V}$, where $\bar{V} = \frac{1}{n} \sum_{i=1}^n v_i$ is the seasonal mean average of MJJA for each year. Thus, the analysis removed the seasonal mean, and the higher EOFs

explain the sub-seasonal variability. EOF analyses characterize the statistical modes of variability of the GP-LLJ [44]. The GP-LLJ statistical modes of variability were obtained from both 1-day and 5-day time series sampling frequencies over the domain (15° – 50° N; 110° – 75° W) for the sub-seasonal and interannual scales, respectively. Both the daily and 5-day fields were previously band-pass filtered on the sub-seasonal scale (10- to 60-day). This band-pass filtering process was performed independently each year using a length from 1 May through 1 September. For the interannual variability, we computed the 5-day sampling frequency after band-pass filtering for each year from 1982 to 2014. The filtering approach helped show whether the CFS-RR at the sub-seasonal scale could simulate the variability of the GP-LLJ as the first EOF mode described by the NARR. As in [27], the EOF1 and EOF2 show the GP-LLJ wet and dry modes of variability, respectively. The GP-LLJ index was defined as the temporal principal component (PC) of the NARR and the CFS from 900 mb meridional wind during the summer MJJA. The spatial patterns in this paper were denominated as EOFs and the temporal patterns (or time series) as PCs [43].

2.2.2. The CGT Index

The NGP precipitation response to upper-level atmospheric was evaluated using spatial and temporal correlations between the GP-LLJ temporal index and 200 mb geopotential height (HGT) anomalies. Also, we applied the EOF analysis to a 200 mb geopotential height to identify the CGT large-scale atmospheric pattern linked with the temporal variability and spatial distribution of precipitation and the GP-LLJ. This study explored the spatiotemporal variation of the HGT and the CGT index. The first pattern of variability emerged from the spatiotemporal variability of the CGT index, which was reconstructed by the HGT's EOF2 and PC2 ($\tilde{HGT} = \text{EOF2} \times \text{PC2}$). The second pattern of variability emerged from the EOF1 of 10- to 60-day band-pass-filtered HGT anomalies for all cases. These patterns of variability enabled the systematic evaluation of CGT as the dominant pattern of variability. The consequent correlations and EOF maps (see Section 3.1) represent the spatial coherence of variability between observations and simulations, quantified by the spatial correlation between a limited domain. To systematically identify the CGT as the dominant mode of variability for each simulation, we applied a 10- to 60-day band-pass filter. This step guaranteed that EOF1 is CGT's dominant statistical mode [45]. The multi-taper method (MTM) identifies the significant spectral peaks in the temporal PCs and time series [46].

2.2.3. The Thirty-Day Forecast of the CFS

The forecasts of 30-day precipitation, computed from the CFS reforecast [36], revealed significant insights. The nine-month CFS simulations were used for the entire period from 1982 through 2009, which is the study period. We computed a precipitation index (NGP precipitation) to compare observed and simulated precipitation; the NGP precipitation is defined as the average precipitation over the NGP region (37.5° – 45° N and 103° – 90° W; see the box in Figure 1). We used the initialization at 12Z from 1 May through 1 September each year for all the CFS cases. To assess the predictability skill of CFS-R (in forecast mode), we used a correlation analysis between the observed and simulated GP-LLJ and CGT indices. We analyzed the forecast skill of precipitation based on the GP-LLJ and the CGT indices for a 30-day timespan. Here, both retrospective and reforecast simulations applied the same analyses. For the reforecast cases, we used a 90-day window to compute the statistical EOF of v-wind and HGT and ensure the integration of the sub-seasonal signals. We used the Pearson correlation between the CFS and observed NGP daily precipitation to evaluate the simulation skill.

2.2.4. Spatial and Temporal Attributions

The selected simulations of the GP-LLJ are those with statistically significant Pearson correlation coefficients between the GP-LLJ index of the NARR and the CFS-R for a 30-day range after the forecast initialization. We used the spatial correlation between the PC1 of the 900 mb meridional wind and the geopotential height to diagnose CGT at 200 mb. Changes

in PC1—in the 30-day Hövmoller diagram over the 40°–50° N latitudinal average—support the statistical significance of the correlations as one of the criteria for pattern emergence from the principal components analysis. The second criterion is that all cases from 1982 to 2009 show the significant cases that occurred when the GP-LLJ and CGT correlate with the already characterized patterns using the retrospective reanalysis cases. While the individual t-statistics test estimated the local significance at each grid point, the collective significance was evaluated using the method of field significance [47]. The implementation of this method used randomization of every grid point, with 1000 Monte Carlo sampling, to compute a non-parametric distribution to assess the collective significance of the spatial patterns.

Correlation threshold selection

We selected the cases in which the correlation was statistically significant and reached values higher than the estimated correlation threshold selection according to a non-parametric approach. The selection used a non-parametric distribution constructed by randomizing the original sequence of the time series using a bootstrap approach [44]. This distribution is the null distribution for testing the selected threshold. A bivariate normal distribution for two variables like GP-LLJ index and NGP precipitation is used, as follows:

$$f(x, y) = \frac{1}{2\pi\sigma_x\sigma_y\sqrt{1-\rho^2}} \exp\left\{-\frac{1}{2(1-\rho^2)} \left[\left(\frac{x-\mu_x}{\sigma_x}\right)^2 + \left(\frac{y-\mu_y}{\sigma_y}\right)^2 - 2\rho\left(\frac{x-\mu_x}{\sigma_x}\right)\left(\frac{y-\mu_y}{\sigma_y}\right) \right]\right\}, \quad (1)$$

which explores all the possible conditional realizations. The dimensional variables x and y define the function $f(x, y)$, the mean μ_x and μ_y , and the standard deviations σ_x and σ_y , and ρ is the correlation between x and y . Considering the hypothesis that overlapping GP-LLJ and CGT enhance the predictability of NGP precipitation, we use a multidimensional normal distribution of order three. In other words, this testing assesses the conditional probability of an event happening when another two events have already occurred (e.g., a correlation higher than the threshold value between precipitation and GP-LLJ and CGT). The multivariate normal distribution equation is as follows:

$$f(\mathbf{x}) = \frac{1}{(2\pi)^{K/2} \sqrt{\det[\Sigma]}} \exp\left[-\frac{1}{2} (\mathbf{x} - \boldsymbol{\mu})^T [\Sigma]^{-1} (\mathbf{x} - \boldsymbol{\mu})\right], \quad (2)$$

where $\boldsymbol{\mu}$ is the K-dimensional mean vector of \mathbf{x} , and $[\Sigma]$ is the covariance matrix of \mathbf{x} [44].

3. Results

3.1. Diagnostics of NGP Precipitation, GP-LLJ, and CGT

Our thesis states that concurrent multi-scale climate phenomena improve the predictability of 30-day precipitation, or its absence, linked to extended wet or drought phenomena in the NGP area. We tested the proposed sub-seasonal predictive framework for the precipitation event in 1993 and the consequent flooding event in the NGP. Also, we tested the sub-seasonal predictability of precipitation deficits characteristic of droughts, such as the 1988 event in the same area.

3.1.1. Geospatial Precipitation Pattern Attributions

The spatial distribution of the GP-LLJ and CGT and the associated precipitation across the NGP area were analyzed using NARR data (Figure 3). The EOF analysis showed the spatiotemporal patterns of these variables for the 900 mb meridional wind (V900). The associated temporal PC1 is correlated with precipitation and a 200 mb geopotential height. The V900 EOF1 shows the GP-LLJ and represents only 30% of the explained variance for 1993. The core of the GP-LLJ—along with Texas, Oklahoma, and Kansas—shows the same pattern as in other studies [24,27,32,43]. The spatial pattern of correlation (between precipitation and the V900 PC1, Figure 3b) shows a statistically significant positive relation in the north-central United States (Nebraska, Iowa, Minnesota, South Dakota, and North

Dakota) with correlation values higher than 0.4 ($p < 0.05$). This pattern coincides with the region of the maximum precipitation anomaly in Figure 1 and shows the association between the GP-LLJ and NGP precipitation. Simultaneously, the 200 mb HGT correlated with the V900 PC1 showed a high positive anomaly region over the Great Lakes, part of a wave pattern resembling the CGT. As noted by [30,31], this wave pattern reveals a large-scale linkage between continental patterns of precipitation anomalies and the variability of the westerly upper jet stream. The HGT pattern indicated by a complementary EOF analysis with 200 mb HGT anomalies (Figures 4 and S1 with a global domain) that the matching patterns obtained from a second approach using the EOF2. The complementary EOF analysis on the 200 mb HGT showed the CGT as the second dominant pattern (11% of explained variance). Next, we evaluate whether CFS-RR, in a reanalysis mode, can reproduce similar variability for the GP-LLJ and the CGT.

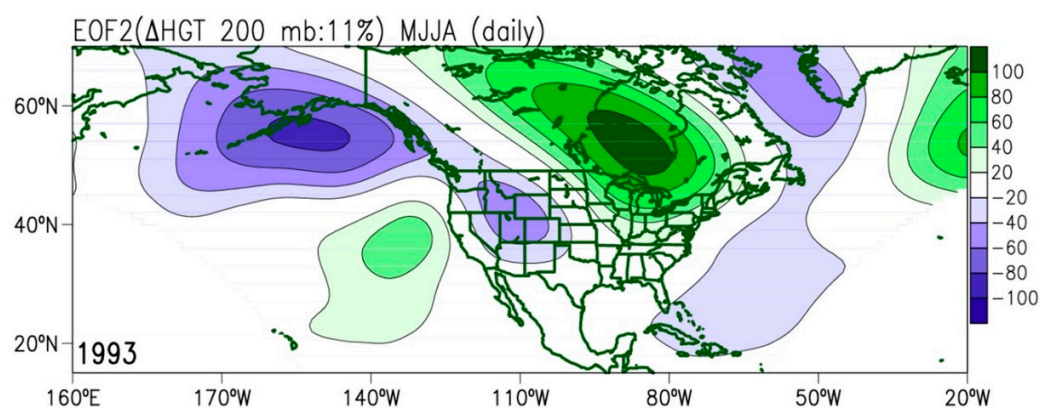


Figure 4. Spatial pattern of the empirical orthogonal function mode 2 (EOF2) from 200 mb geopotential height anomalies (Δ HGT) from the North America regional reanalysis (NARR) obtained from daily fields from 1 May through 1 September (MJJA), 1993, with an explained variance of 11%.

3.1.2. Sub-Seasonal Modes of Variability

The dominant temporal scales of the GP-LLJ, CGT, and NGP precipitation were analyzed with power spectra to identify the temporal ranges of variability (Figure S2). Also, we suggest whether CFS-RR in a reanalysis mode can reproduce the GP-LLJ and CGT variability patterns. The GP-LLJ index (V900 PC1) had a dominant 6-day spectral signal, the GCT index (HGT200 PC2) showed a band at 10–60 days, and precipitation presented both. This result indicates that the dominant temporal modes vary in the daily (6 days) and sub-seasonal (10–60 days) scales, which are statistically significant at the 95% level of confidence (Figures S2 and S3). In Figure 5, the Hövmoller diagram for 1993 along 102° – 90° W depicts the relationship among precipitation (shaded), the GP-LLJ index (magenta line), and the CGT index (green line). It reveals the coherent variability of the GP-LLJ index at a high frequency and the CGT at a low frequency. With arrows, Figure 5 highlights CFS precipitation's forecast cases, with a correlation above 0.35 (compared with observed precipitation). These instances coincide with the maxima of EOF's meridional winds at 900 mb and EOF's 200 mb geopotential height. This result illustrates cases in which the magnitude of the GP-LLJ index and the phase transition indicated by the CGT index might play an essential role in the predictability skill of NGP precipitation.

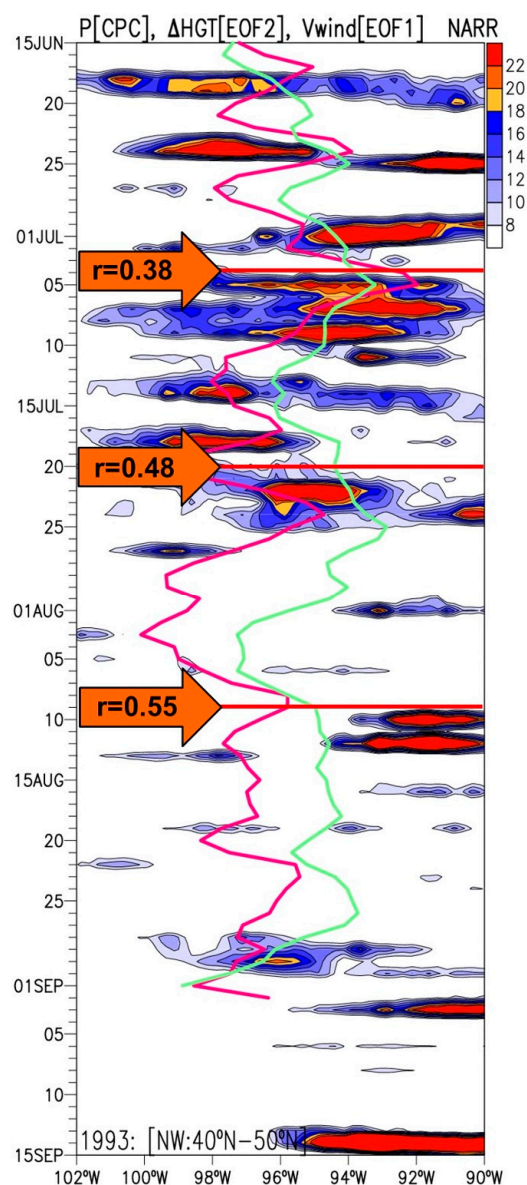


Figure 5. Longitudinal-time Hövmöller diagram of observed precipitation for the 1993 summer season. The longitudinal average is taken over 40° N–50° N. Superimposed solid lines are the GP-LLJ index (magenta) and CGT index (green), which were obtained using empirical orthogonal function analysis using the North American Regional Reanalysis (NARR). Big arrows and horizontal lines are added to indicate the cases of high CFS precipitation correlation.

3.1.3. Interannual Modes of Extended Precipitation and Drought

The analysis of EOF on the wind speed at 900 mb on the CFS-RR and NARR datasets has shown the ability of both products to capture the underlying mechanisms of precipitation surplus and deficit in the NGP. The patterns of interannual variability of V-900 emerge from the EOF analysis applied to the NARR and CFS-R datasets for 1979–2010 and 1979–2014, respectively (these periods coincided with the observations). In Figure 6, the dominant EOF1 and EOF2 spatial patterns obtained from NARR and CFS-RR indicate GP-LLJ’s wet and dry climate regimes. In our analyses, the wet mode (EOF1) and the dry mode (EOF2) contribute 26% and 19% to the total variability, respectively, consistent with [32]. Additional analyses reveal that the CFS-RR contributes similarly to the total variability (Figure 6b). While the CFS-RR shows statistically similar results as the NARR, some minor differences between both products might be due to loading the two leading

PCs. In the CFS-RR, the explained variance for the wet mode (EOF1) is 23% and for the dry mode (EOF2) is 18%. Based on the results above, the CFS simulates the GP-LLJ's moisture transport mechanisms of the Gulf of Mexico by enhancing it in the wet-EOF mode and suppressing it in the dry-EOF mode. The results indicate that the CFS-RR simulates the interdependence between NGP precipitation, the GP-LLJ, and the CGT, as in the 1993 flood and 1988 drought events. The sources of predictability of extreme rainfall might be more evident than those for drought. The latter indicates chronic or interannual water deficits, which require further analysis. We explore the 1988 drought using the EOF1 for 850 mb meridional wind (v_{850}). The V_{850} correlated with precipitation (for coefficients between 0.45 and 0.55 during the 30-day range starting on July 15), confirming the dry GP-LLJ mode under drought (Figure S4). In the section below, we use a modeling framework in a forecast mode to illustrate how GP-LLJ and CGT are simulated for a 30-day precipitation forecast time.

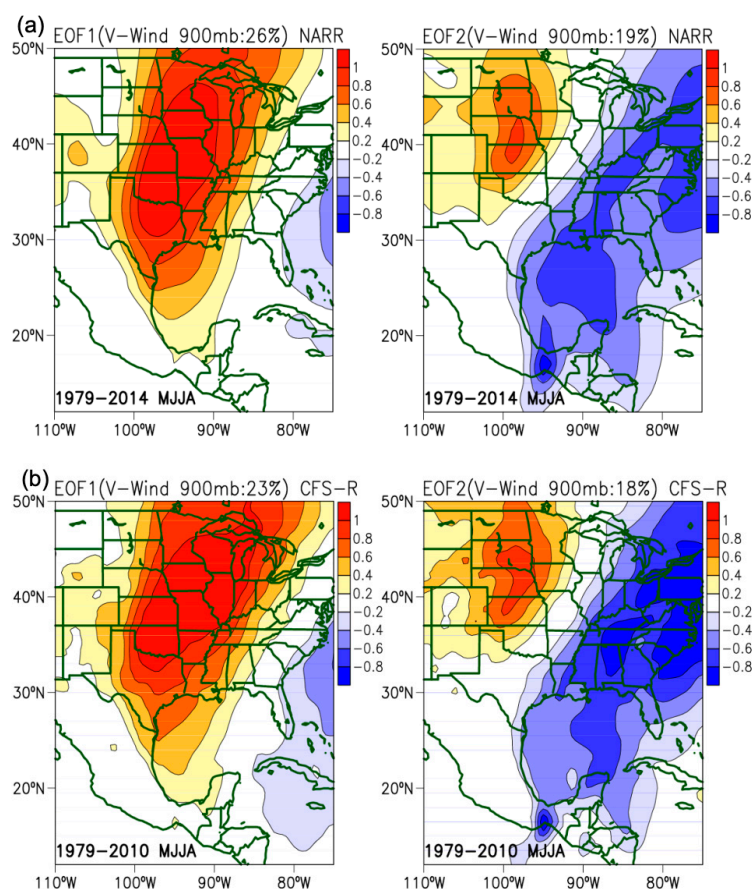


Figure 6. Spatial patterns of the two dominant empirical orthogonal functions (EOF1 and EOF2) of 900 mb meridional wind for (a) the North American Regional Reanalysis (NARR) and (b) the Climate Forecast System retrospective reanalysis (CFS-RR). Both were obtained from the periods 1979–2014 and 1979–2010. The explained variance of these EOFs is shown in percentage at the top of each graph.

3.2. Sources of NGP Precipitation Predictability

We further examined the relationship among GP-LLJ, CGT, and NGP precipitation in a forecast mode (CFS-R) at the daily and sub-seasonal scales. A particular interest was identifying whether precipitation predictability is enhanced when the CFS-R captures GP-LLJ and CGT during the initialization process. As a testing example, we evaluated the forecast skill of simulated precipitation over the NGP for 1988 and 1993 using temporal correlation for a 30-day timespan (Table 1). The selection of cases was based on unidimensional and multidimensional distributions for continuous correlation thresholds. These analyses indicated the unconditional and conditional probability distributions for an

improved predictive skill for NGP precipitation, GP-LLJ, and CGT. In the unidimensional case (Figure 7), a 0.4 correlation threshold at 95% suggests that the three variables are unlikely to be generated as a random process. When NGP precipitation is attributed to GP-LLJ or CGT, the bi-dimensional conditional distribution indicates that the probability of precipitation can be attributed to the occurrence of the regional- to large-scale climate phenomena presented here (Figure 8). The third case supports the central hypothesis of this study, meaning that the multidimensional conditional distribution—the rising probability of NGP precipitation when both GP-LLJ and CGT occur—likely leads to improvements in the predictive skill above a given correlation threshold (Figure 9).

Table 1. The Pearson correlation for the precipitation index (NGP precipitation), the Great Plains low-level jet (GP-LLJ) index, and the circumglobal teleconnection (CGT) index between the Climate Forecast System reforecast (CFS-R) and the North American Regional Reanalysis (NARR) for 30 days of simulations. The initial simulation time is indicated in the first column, and statistically significant results ($p < 0.05$) are bolded. The correlation values were aggregated for 100° – 60° W region, as observed in Figure S6.

Model Initialization	NGP Precipitation	GP-LLJ Index	CGT Index
11 May 1988	0.44	0.14	0.12
21 May 1988	0.77	0.36	0.13
25 June 1988	0.46	0.21	0.31
30 June 1988	0.37	0.39	0.57
15 July 1988	0.36	0.38	−0.33
9 August 1988	0.42	0.36	−0.39
5 July 1993	0.38	0.71	0.12
20 July 1993	0.48	0.60	0.3
9 August 1993	0.55	0.56	−0.22
14 August 1993	0.38	0.57	0.29
24 August 1993	0.45	0.01	0.12

With the attributions and the correlation threshold selected (above 0.35), we evaluated the correlation between NGP precipitation and the modeling and forecast products. Table 1 shows the correlation between NARR (observed) and CFS-R (reforecast) precipitation for only eleven cases. Individual precipitation cases perform well (with $r > 0.35$), as some other cases show low correlation coefficients (Figure S5 shows two examples of simulated precipitation), like what [36] reported. Table 1 also shows the correlation among the CFS-R, GP-LLJ, and CGT for the observed and forecast precipitation datasets. The forecasting skill of the CGT was evaluated by correlating the HGT patterns from the 100° – 60° W region evolving 30 days, as shown in the Hövmoller diagram in Figure S6. This figure shows the temporal evolution of the dominant patterns of low and high values of HGT. The HGT emerged patterns based on EOF1 and EOF2 indicate that the CGT is the dominant mode of variability. The forecast-based patterns and phase transitions were comparable to those in NARR.

The relationship among the GP-LLJ, CGT, and NGP precipitation (Figures 5 and S6) was expanded to the entire CFS-R simulations from 1982 to 2009 and synthesized in Figures 10 and 11. These figures synthesize the 30-day correlation analyses of precipitation between the CFS-R and NARR for all the cases. The location of the boxes represents the forecast time of initialization and, inherently, the randomness of the cases. For MJJ only, we found that a total of 126 cases of NGP precipitation (Figure 10; 22.9% of the total analyzed) correlate (values higher than 0.35 and $p < 0.05$) in the 30-day range. For an extended MJJA, 154 cases represented 21%, indicating no significant changes. From the first set, 40.5% (51) of cases showed correlation values higher than 0.5. We selected the threshold based on [44]

multidimensional probability distribution. The analysis used this pool of cases (22.9%) to assess the CGT and the GP-LLJ's role in NGP precipitation.

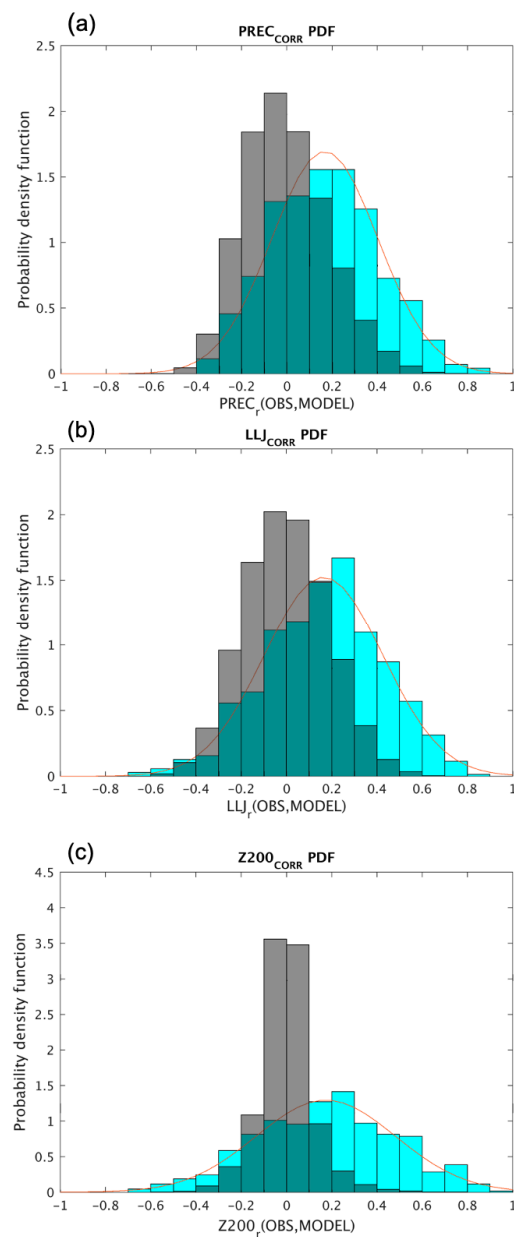


Figure 7. Unconditional probability density functions (PDF) of the correlation values for the following three indices: NPG precipitation (a), GP-LLJ index (b), and CGT index (c)—cyan bars. The total number of cases for each distribution is 701, and the continuous line is the fitted normal PDF. The x-axis represents the correlation values between the observation and reanalysis and the forecasted value from CFS-R for each index, respectively. The null distribution (gray bars) is constructed by bootstrap of this pool of cases and with a randomization of the original time series before computing the correlation.

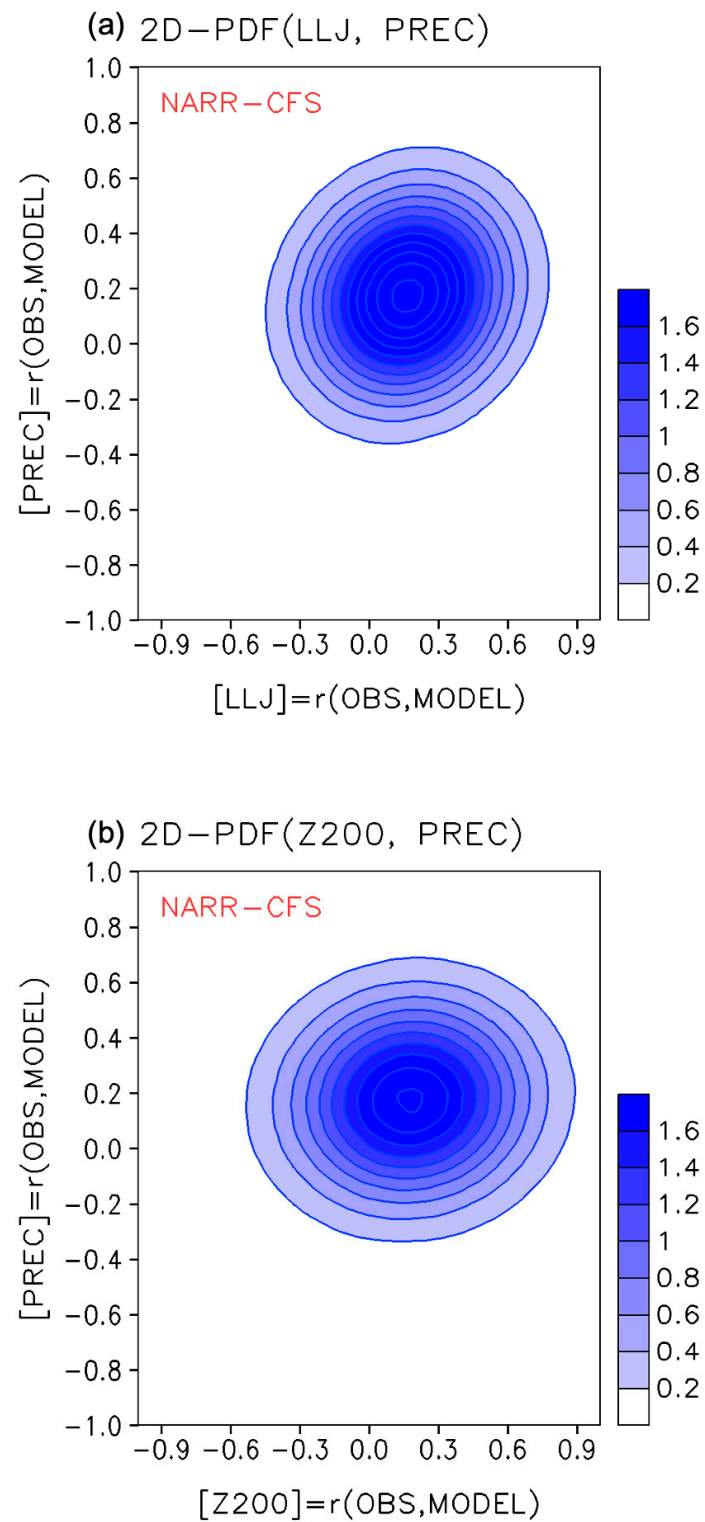


Figure 8. Conditional bi-dimensional probability distribution (2D-PDF) constructed with Equation (2) for the following two pairs of datasets: (a) the GP-LLJ and NGP precipitation and (b) the CGT index and NGP precipitation (Z200, PREC). The data represent the total available cases between 1982 and 2009 (701 cases).

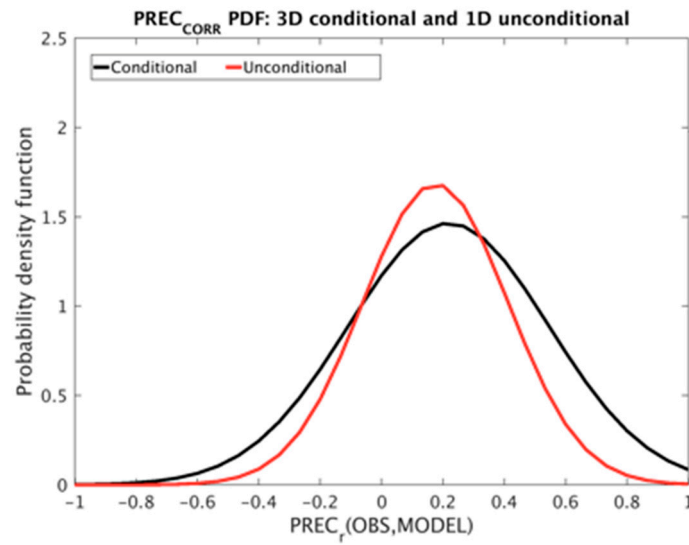


Figure 9. The conditional and unconditional probability distribution of correlation for the NGP precipitation. The x -axis is the precipitation correlation values between observation and CFS-R for 1982–2009 based on 701 cases. The unconditional distribution is a one-dimensional PDF, the same as in Figure S5a, which is added here for comparison. The conditional distribution is based on the simultaneous occurrence of GP-LLJ and CGT threshold, computed with Equation (2) in the text. The conditional probability is plotted for the following condition: [GP-LLJ index] r (NARR, CFS-R) > 0.4 and [CGT index] r (NARR, CFS-R) > 0.4.

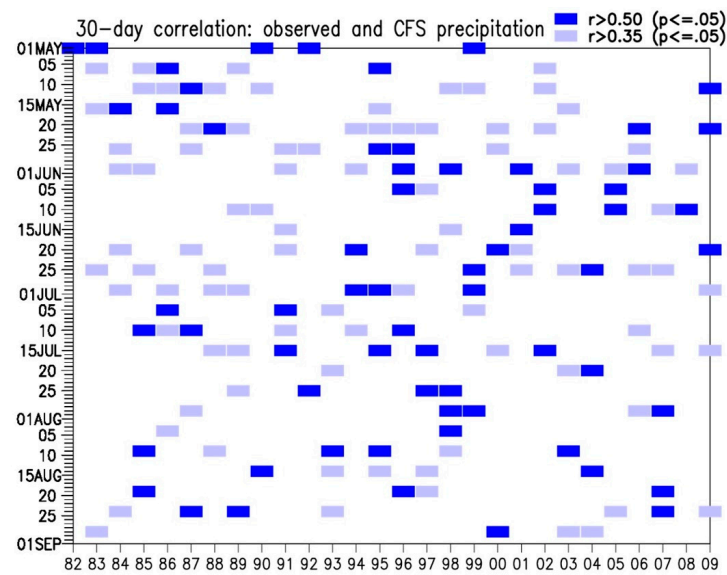
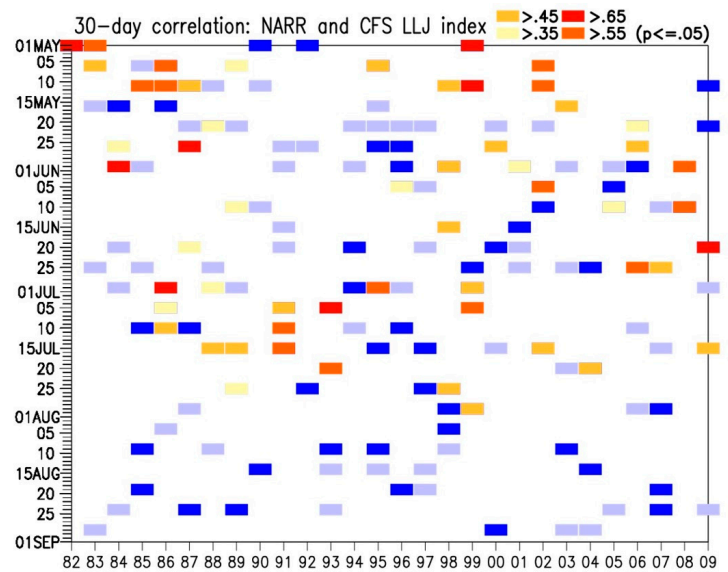
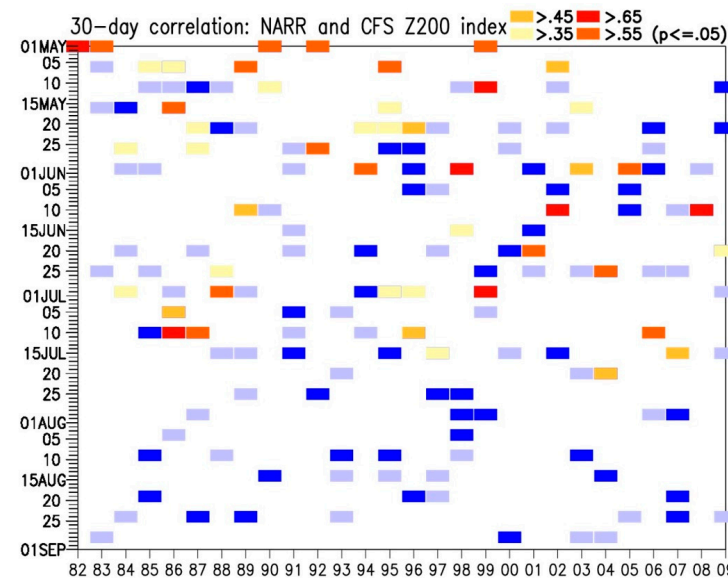


Figure 10. Thirty-day Pearson temporal correlation between observed precipitation and the Climate Forecast System reforecast (CFS-R) precipitation for an area average over the Northern Great Plains (37.5°–45° N; 103°–90° W) described using blocks in two colors. The light-blue blocks represent statistically significant correlations higher than 0.35 but lower than 0.5, and the dark blue blocks represent correlations higher than 0.5. Unfilled spaces have correlation values lower than 0.35. The location of the block defines the initialization of the CFS-R. The analysis season is from 1 May through 1 September from 1982 to 2009.



(a)



(b)

Figure 11. As in Figure 10, the Great Plains low-level jet (GP-LLJ) index correlation between the North American Regional Reanalysis (NARR) and the Climate Forecasting System reforecast (CFS-R) simulations for 1982–2009. (a) Correlations are shown only for the statistically significant precipitation cases, as defined in Figure 10. These correlations are noted in this plot with the same light blue and dark blue blocks when the LLJ correlation is not significant. Statistically significant correlations are classified into four groups using the following ranges: 0.35, 0.45, 0.55, and 0.65 in orange tones. Only cases from 1 May through 31 July were analyzed. (b) Correlation for the 200 mb geopotential height index (Z200) between the North American Regional Reanalysis (NARR) and Climate Forecasting System (CFS) simulations.

The 30-day correlation analyses—the GP-LLJ indices and 200 mb HGT anomalies (Figure 11a,b)—are shown for the cases in which simulated precipitation was significantly correlated ($r > 0.35$; blue blocks in Figure 10), and only from May through July (MJJ). Categories for the cases were split into four groups according to the correlation value, such as $r > 0.35$, $r > 0.45$, $r > 0.55$, and $r > 0.65$. Of a total of 126 selected cases, 55 (43.6%) were able to appropriately simulate the GP-LLJ (Figure 11a) and 47 (37.3%) were able to

simulate the CGT (Figure 11b), which is like what occurs in Table 1. These 43.6% and 37.3% represent the CFS's skill to simultaneously reproduce the GP-LLJ and the CGT, showing their importance to the predictability of NGP precipitation. This analysis' important caveat is that the selected cases were limited to 9% of the total possible in the CFS-R (121 cases). This sampling population could be fixed by including a multi-model analysis. However, this extra analysis is beyond the scope of this study.

4. Discussion

We have evaluated the sub-seasonal predictability of precipitation by addressing the following two scientific questions: How strong is the link between the GP-LLJ and CGT in a modeling framework concerning summer precipitation over the Northern Great Plains? Furthermore, how does precipitation predictability vary when the internal dynamics of a GCM capture these two modes of climate variability?

The first question was answered by showing the GP-LLJ and CGT's role in the variability of NGP precipitation at sub-seasonal and interannual scales. As indicated by [24–26] for summer precipitation, the link among the GP-LLJ, CGT, and NGP precipitation is strong, as shown by the NARR and CFS-RR using EOF analysis and Pearson correlation. In both reanalyses, the GP-LLJ contributes to the rainfall variability in the NGP on a daily scale, as expected after the results from [26,32]. The EOF analysis of V900 for the NARR for 30 years identifies typical patterns of spatiotemporal variability for the GP-LLJ, as expected after [27]. The EOF analysis on 200 mb HGT reveals the CGT as the second dominant pattern for the precipitation in the NGP, which agrees with [30]. We have found that the association among precipitation, GP-LLJ, and CGT occurs at the daily and sub-seasonal scales. Thus, NGP precipitation responds to regional to global moisture transport mechanisms in the lower troposphere. At the same time, the CGT at the sub-seasonal scale modulates these mechanisms.

We used the GP-LLJ, CGT, and NGP precipitation relationship as a metric to evaluate their role in a forecasting framework. Our analysis of precipitation depicts how the GP-LLJ peaks coincide with major convective storms. The correlation values between both are statistically significant, which confirms previous research using alternative techniques [26]. Similarly, the CGT index reveals a statistically significant link with GP-LLJ with a 0.5 ($p < 0.05$) correlation between them. Thus, the GP-LLJ, CGT, and NGP precipitation relationship facilitates a metric to evaluate the 30-day predictability of precipitation. Our proposed analysis indicates how this relationship is maintained in space (by the CGT index) and time (by the GP-LLJ index). This process-based approach could incorporate the predictability of the dominant drivers of precipitation into the analysis.

For the second question, we found that the 30-day NGP precipitation can lead to more accurate forecasts when evaluated in the context of the GP-LLJ and CGT relationship maintained in space and time. A study by [48] concluded that correct simulation of the GP-LLJ is necessary, but more is needed to represent NGP precipitation adequately. As hypothesized here, precipitation forecast skill increases in response to the enhanced simulation of the GP-LLJ and CGT at daily and sub-seasonal scales. We found that the improved performance of the CFS precipitation in a forecast mode is due to the proper simulation of the GP-LLJ–CGT individual cases. At least 43% of the selected “good” cases outperform when adequately representing the GP-LLJ and the CGT. Thus, it gives an objective process-based approach to quantify the role of these two modes of climate variability. Precipitation prediction is better when the relationship between these two climate variables is maintained.

The CFS, in a forecast mode, simulates limited cases of 30-day precipitation ($r > 0.5$ [$p < 0.05$]). Our study has found that 126 cases (22.9% of the total analyzed) were able to reach a 30-day precipitation correlation higher than 0.35 ($p < 0.05$). In addition, from this group, 40.5% show correlation values higher than 0.5 ($p < 0.05$); therefore, only 9% of the total simulated cases. A similar range of improvement can be found when the GP-LLJ and CGT have the same thresholds. From the total 126 selected cases, 43.6% were able to

simulate the GP-LLJ, and 37.3% of the CGT exceeded the threshold ($r > 0.35$, [$p < 0.05$]). These 43.6% and 37.3% of the cases demonstrate the importance of the GP-LLJ and CGT link for the predictability of NGP precipitation. Our further analysis of the multidimensional covariance with a three-dimensional PDF confirms that high precipitation correlation coefficients are associated with a better predictive GP-LLJ and CGT. The authors of [27] highlighted how essential the GP-LLJ is in the NGP precipitation. However, this research demonstrates that predictability is improved when CFS adequately simulates the GP-LLJ and the CGT signals, but we did not explore the physical mechanism. As the temporal variability of the CGT is higher in the range of 10–60 days, the CGT provides predictability in these cases. However, it is essential to consider the 6-day variability of the GP-LLJ, which plays a secondary role in extending the range of precipitation predictability to 30 days.

The GP-LLJ and CGT analysis suggests that its link is passed through the model during initialization. This model ability was confirmed with the CFS evaluation using its reanalysis version, as perfect boundary conditions enable the modeling framework to efficiently simulate the GP-LLJ and CGT at the sub-seasonal and interannual scales. This important outcome confirms that the well-known dilemma initialization process is critical [49]. Thus, rainfall generation in the NGP in GCMs is not independent of the initial conditions and might be model-dependent, so it is interesting to explore in a multi-model version [3]. This condition may indicate substantial uncertainty in the modeling evolution of the GP-LLJ and CGT flux, but the large-scale flow well informs a few regional weather patterns.

Although the CFS-R, as analyzed by [36], showed meager predictability skill on average, this study showed that individual cases could reach higher skill levels when separated by how two significant drivers simulate NGP precipitation. Improved predictability of precipitation occurs when CFS adequately simulates the GP-LLJ and the CGT. In this context, predictability is limited to a few cases within what [50] call “windows of opportunities”. This outcome could motivate researchers to explore the initialization process of those dominant modes of variability further or how the GP-LLJ–CGT link could be built into the internal dynamic of the modeling framework. The author of [31] found that the CGT has two modes of variability that influence U.S. precipitation. This study encourages researchers to continue exploring how these two climate modes affect precipitation’s sub-seasonal to seasonal predictability within the challenging 30-day time [51]. The combined use of these modes of variability in a forecasting system could potentially improve predictive frameworks for water resources management and governance [19,52], phenotype predictability [22,53], water supply and demands for agriculture [54–56], infrastructure risk, and resilience [20,57]. Furthermore, the characterization of integrated variables, such as soil moisture, can enhance the diagnostics and prognostics of extreme events associated with precipitation [58–60].

5. Conclusions

This study identifies the importance of the interaction between regional (GP-LLJ) and global-scale (CGT) sources on 30-day forecasted precipitation. Here, we documented how these two sources contribute to the predictability of precipitation in the NGP. However, we acknowledge that the GP-LLJ and CGT can be limited in the number of cases, and more sources are still required to be analyzed. Additionally, our study shows promising results for expanding the approach to a multi-variable technique (i.e., with machine learning). Although we have found that the interaction occurs at the daily (GP-LLJ) and sub-seasonal (CGT) scales, we did not identify which source plays a leading role in the sub-seasonal predictability of precipitation in the Northern Great Plains. The answer to this question may be related to the assessment of the amplitude of forecasted precipitation (for example, extreme precipitation predictability differs from average precipitation). The analysis of the CFS forecast suggests that the ability to accurately forecast sub-seasonal precipitation increases when the simulations of the GP-LLJ and CGT are enhanced. These cases must

be verified with other models or multi-model approaches (i.e., the North American Multi-Model Experiment).

Supplementary Materials: The following supporting information can be downloaded at <https://www.mdpi.com/article/10.3390/atmos15070858/s1>: Figure S1: Spatial pattern of the empirical orthogonal function mode 2 (EOF2) from 200 mb geopotential height anomalies (Δ HGT). The HGT is obtained from the Climate Forecast System (CFS) retrospective reanalysis. The EOF is calculated with daily fields from 1 May through 1 September (MJJJA) of 1993, with explained variance of 6%; Figure S2: Multi-taper method (MTM) power spectrum of the temporal dominant principal components (PC) of both 900 mb meridional wind (V-wind PC1; a) and 200 mb geopotential height anomalies (Δ HGT PC2; b) for the daily period from 1 May through 1 September 1993. MTM power spectrum of precipitation ([P]; c) for the Northern Great Plains precipitation index averaged over the region defined at 37.5–45° N; 103–90° W (MW). The two superimposed lines are the levels of confidence at 95% and 99%; Figure S3: Multi-taper method (MTM) power spectrum of 200 mb geopotential height (a), precipitation (b), and meridional wind at 900 mb (c). The spectrum is calculated for several years indicated in the plot: 2010, 1993, 1998, 2008, and 2010. The time series of each field are averages over different areas for precipitation (37–43° N; 102–90° W), HGT (40–60° N; 90–60° W), and V900 (25–40; 102–95° W). The time series are daily for the period from 1 May through 1 September 1993. The superimposed line is the levels of confidence at the 95% level of confidence for each case; Figure S4: Spatial pattern of the empirical orthogonal function mode 1 (EOF1) from 850 mb meridional wind (V850mb). The V850mb was obtained from the Climate Forecast System (CFS) retrospective reanalysis (CFS-RR). The EOF is calculated with daily fields from 1 May through 1 September (MJJJA) of 1988. A correlation of 0.54 is found between the associated V850 PC1 and the analogous NARR PC1 for a 30-day length after 15 July; this correlation is in the range of [0.45, 0.55], as defined in Figure 9. Also, a correlation of 0.36 is found between this V850 PC1 and NGP precipitation. 1988 is considered a dry year for the Northern Great Plains, as identified by the time in Figure 2b; Figure S5: Longitudinal-time Hövmoller diagram of Climate Precipitation Center (CPC) precipitation averaged among 37° N and 43° N (shaded is the same precipitation plot as in Figure 3). The superimposed black line is the CPC-observed precipitation average over the region 37°–43° N, 102°–90° W. The superimposed red and blue lines are precipitation average over the same as the black line, but for Climate Forecast System (CFS) reforecast simulations starting on 5 July (red line) and 10 July (blue line); Figure S6: Hövmoller spatiotemporal variability of a reconstructed 200 mb geopotential height anomaly (Δ HGT). (a) Using the second empirical orthogonal function (EOF2) mode. The superimposed green line is the PC2 associated with this mode. (b) Using the EOF1 mode with original NARR HGT data previously filtered with a 10- to 60-day band-pass filter. (c) Using EOF1 mode 1 (also previously filtered with a 10- to 60-day band-pass filter) from the Climate Forecast System reforecast (CFS-R). Boxes represent the region of correlation analysis; Table S1: List of acronyms.

Author Contributions: Conceptualization, C.M.C. and F.M.-A.; methodology, C.M.C. and F.M.-A.; software, C.M.C. and F.M.-A.; validation, C.M.C. and F.M.-A.; formal analysis, C.M.C. and F.M.-A.; investigation, C.M.C. and F.M.-A.; resources, F.M.-A.; data curation, C.M.C.; writing—original draft preparation, C.M.C. and F.M.-A.; writing—review and editing, C.M.C. and F.M.-A.; visualization, C.M.C.; supervision, C.M.C. and F.M.-A.; project administration, F.M.-A.; funding acquisition, F.M.-A. All authors have read and agreed to the published version of the manuscript.

Funding: This study was funded by the U.S. Department of Agriculture (USDA) Agriculture and Food Research Initiative Grant number NEB-21-176 and NEB-21-166 from the National Institute of Food and Agriculture, Plant Health and Production and Plant Products: Plant Breeding for Agricultural Production, the U.S. Geological Survey (USGS), the Daugherty Water for Food Global Institute (DWFI) at the University of Nebraska-Lincoln (UNL), and the UNL's Layman Award.

Institutional Review Board Statement: Not applicable.

Informed Consent Statement: Not applicable.

Data Availability Statement: All data sources are cited through the text and listed in the References section. Additional data can be found at <https://zenodo.org/records/5784508> (accessed on 19 July 2024) [61] ("Precipitation, low-level jet, and geopotential height data for analyzing sources of predictability in the US Northern Great Plains: DOI 10.5281/zenodo.5784508").

Acknowledgments: We thank the U.S. Department of Agriculture (USDA) Agriculture and Food Research Initiative Grant number NEB-21-176 and NEB-21-166 from the National Institute of Food and Agriculture, Plant Health and Production and Plant Products: Plant Breeding for Agricultural Production, the U.S. Geological Survey (USGS), the Daugherty Water for Food Global Institute (DWFI) at the University of Nebraska-Lincoln (UNL), and the UNL's Layman Award. Also, we are grateful to the Earth System Research Laboratory at NOAA for providing the gridded data. Also, the Climate Forecast System (CFS) retrospective reanalysis and reforecast dataset were obtained from the National Centers for Environmental Prediction (NCEP). We are grateful to the UNL Holland Computer Center for access to their high-computing facilities to perform the analysis, the code for which can be found at <http://bit.ly/GP-LLJ> (accessed on 19 July 2024). Finally, we appreciate the time, feedback and comments provided by the reviewers and the academic editor.

Conflicts of Interest: The authors declare no conflicts of interest.

References

1. USGCRP. U.S. Climate Modeling Summit (USCMS), 2023: The Ninth U.S. Climate Modeling Report. NOAA Center for Weather and Climate Prediction, College Park, MD. Available online: https://www.globalchange.gov/sites/default/files/documents/igim/USCMS_2023_Summit_Report.pdf (accessed on 1 December 2023).
2. National Oceanic and Atmospheric Administration-National Weather Service. Climate Prediction Center Official 30-Day Forecast. 2024. Available online: <https://www.cpc.ncep.noaa.gov/products/predictions/30day/> (accessed on 10 January 2024).
3. Kirtman, B.P.; Min, D.; Infanti, J.M.; Kinter, J.L.; Paolino, D.A.; Zhang, Q.; Dool, H.v.D.; Saha, S.; Mendez, M.P.; Becker, E.; et al. The North American Multimodel Ensemble: Phase-1 Seasonal-to-interannual prediction; Phase-2 Toward developing intraseasonal prediction. *Bull. Am. Meteorol. Soc.* **2014**, *95*, 585–601. [[CrossRef](#)]
4. Vitart, F.; Ardilouze, C.; Bonet, A.; Brookshaw, A.; Chen, M.; Codorean, C.; Déqué, M.; Ferranti, L.; Fucile, E.; Fuentes, M.; et al. The sub-seasonal to seasonal prediction (S2S) project database. *Bull. Am. Meteorol. Soc.* **2016**, *98*, 163–173. [[CrossRef](#)]
5. Chikamoto, Y.; Timmermann, A.; Widlansky, M.J.; Balmaseda, M.A.; Stott, L. Multi-year predictability of climate, drought, and wildfire in southwestern North America. *Sci. Rep.* **2017**, *7*, 6568. [[CrossRef](#)] [[PubMed](#)]
6. L'heureux, M.L.; Tippett, M.K.; Becker, E.J. Sources of Sub-seasonal Skill and Predictability in Wintertime California Precipitation Forecasts. *Weather. Forecast.* **2021**, *36*, 1815–1826. [[CrossRef](#)]
7. Huang, H.; Patricola, C.M.; Bercos-Hickey, E.; Zhou, Y.; Rhoades, A.; Risser, M.D.; Collins, W.D. Sources of Sub-seasonal-To-Seasonal Predictability of Atmospheric Rivers and Precipitation in the Western United States. *J. Geophys. Res. Atmos.* **2021**, *126*, e2020JD034053. [[CrossRef](#)]
8. Hoerling, M.; Eischeid, J.; Kumar, A.; Leung, R.; Mariotti, A.; Mo, K.; Schubert, S.; Seager, R. Causes and predictability of the 2012 Great Plains drought. *Bull. Am. Meteorol. Soc.* **2014**, *95*, 269–282. [[CrossRef](#)]
9. Johnson, G.P.; Holmes, R.R., Jr.; Waite, L.A. The Great Flood of 1993 on the upper Mississippi River—10 years later. U.S. Geological Survey Information Sheet, 6 p. 2003. Available online: <https://pubs.usgs.gov/fs/2004/3024/report.pdf> (accessed on 19 July 2024).
10. Smith, A.B.; Katz, R.W. U.S. Billion-dollar Weather and Climate Disasters: Data Sources, Trends, Accuracy and Biases. *Nat. Hazards* **2013**, *67*, 387–410. [[CrossRef](#)]
11. United States Department of Agriculture-National Agriculture Statistics Service (NASS). Available online: <https://www.nass.usda.gov> (accessed on 2 December 2023).
12. Garber, K. Midwest Floods Ruin Crops. U.S. News. 2008. Available online: <https://www.usnews.com/news/national/articles/2008/06/18/midwest-floods-ruin-crops> (accessed on 2 December 2023).
13. National Corn Growers Associations (NCGA). Available online: www.worldofcorn.com (accessed on 3 December 2023).
14. United States Department of Agriculture-National Agriculture Statistics Service (NASS-Census). Available online: https://www.nass.usda.gov/Publications/AgCensus/2017/Online_Resources/Ag_Census_Web_Maps/index.php (accessed on 3 December 2023).
15. Ou, G.; Munoz-Arriola, F.; Uden, D.R.; Martin, D.; Allen, C.R.; Shank, N. Climate change implications for irrigation and groundwater in the Republican River Basin, USA. *Clim. Chang.* **2018**, *151*, 303–316. [[CrossRef](#)]
16. Uden, D.R.; Allen, C.R.; Munoz-Arriola, F.; Ou, G.; Shank, N. A Framework for Tracing Social-Ecological Trajectories and Traps in Intensive Agricultural Landscapes. *Sustainability* **2018**, *10*, 1646. [[CrossRef](#)]
17. Amaranto, A.; Pianosi, F.; Solomatine, D.; Corzo, G.; Muñoz-Arriola, F. Sensitivity Analysis of Hydroclimatic Controls of Data-driven Groundwater Forecast in Irrigated Croplands. *J. Hydrol.* **2020**, *587*, 124957. [[CrossRef](#)]
18. Sarzaeim, P.; Muñoz-Arriola, F.; Jarquin, D. Analytics for climate-uncertainty estimation and propagation in maize-phenotype predictions. In Proceedings of the 2020 ASABE Annual International Meeting, Omaha, NE, USA, 12–15 July 2020. Paper No. 1165. [[CrossRef](#)]
19. Muñoz-Arriola, F.; Abdel-Monem, T.; Amaranto, A. Common pool resource management: Assessing water resources planning processes for hydrologically connected surface and groundwater systems. *Hydrology* **2021**, *8*, 51. [[CrossRef](#)]

20. Sarzaeim, P.; Ou, W.; de Oliveira, L.A.; Munoz-Arriola, F. Flood-Risk Analytics for Climate-Resilient Agriculture Using Remote Sensing in the Northern High Plains. In *Geo-Extreme 2021*; ASCE: Reston, VA, USA, 2021; pp. 234–244. [[CrossRef](#)]
21. Sarzaeim, P.; Muñoz-Arriola, F.; Jarquín, D. Climate and genetic data enhancement using deep learning analytics to improve maize yield predictability. *J. Exp. Bot.* **2022**, *73*, 5336–5354. [[CrossRef](#)] [[PubMed](#)]
22. Sarzaeim, P.; Muñoz-Arriola, F.; Jarquin, D.; Aslam, H.; Gatti, N.D.L. CLIM4OMICS: A geospatially comprehensive climate and multi-OMICS database for maize phenotype predictability in the United States and Canada. *Earth Syst. Sci. Data* **2023**, *15*, 3963–3990. [[CrossRef](#)]
23. Livneh, B.; Rosenberg, E.A.; Lin, C.; Nijssen, B.; Mishra, V.; Andreadis, K.M.; Maurer, E.P.; Lettenmaier, D.P. A long-term hydrologically based dataset of land surface fluxes and states for the conterminous United States: Update and extensions. *J. Clim.* **2013**, *26*, 9384–9392. [[CrossRef](#)]
24. Bonner, W.D. Climatology of the low level jet. *Mon. Weather. Rev.* **1968**, *96*, 833–850. [[CrossRef](#)]
25. Bell, G.D.; Janowiak, J.E. Atmospheric circulation associated with the Midwest floods of 1993. *Bull. Am. Meteorol. Soc.* **1995**, *76*, 681–695. [[CrossRef](#)]
26. Arritt, R.W.; Rink, T.D.; Segal, M.; Todey, D.P.; Clark, C.A.; Mitchell, M.J.; Labas, K.M. The Great Plains low-level jet during the warm season of 1993. *Mon. Weather. Rev.* **1997**, *125*, 2176–2192. [[CrossRef](#)]
27. Weaver, S.J.; Nigam, S. Recurrent supersynoptic evolution of the Great Plains low-level jet. *J. Clim.* **2011**, *24*, 575–582. [[CrossRef](#)]
28. Kalnay, E.; Kanamitsu, M.; Kistler, R.; Collins, W.; Deaven, D.; Gandin, L.; Iredell, M.; Saha, S.; White, G.; Woollen, J.; et al. The NCEP/NCAR 40-year Reanalysis Project. *Bull. Amer. Meteorol. Soc.* **1996**, *77*, 437–471. [[CrossRef](#)]
29. Mesinger, F.; DiMego, G.; Kalnay, E.; Mitchell, K.; Shafran, P.C.; Ebisuzaki, W.; Jović, D.; Woollen, J.; Rogers, E.; Berbery, E.H.; et al. North American Regional Reanalysis. *Bull. Amer. Meteorol. Soc.* **2006**, *87*, 343–360. [[CrossRef](#)]
30. Ding, Q.; Wang, B. Circumglobal teleconnection in the Northern Hemisphere summer. *J. Clim.* **2005**, *18*, 3483–3505. [[CrossRef](#)]
31. CianCiancarelli, B.; Castro, C.L.; Woodhouse, C.; Dominguez, F.; Chang, H.; Carrillo, C.; Griffin, D. Dominant patterns of U.S. warm season precipitation variability in a fine resolution observational record, with focus on the southwest. *Int. J. Clim.* **2013**, *34*, 687–707. [[CrossRef](#)]
32. Weaver, S.J.; Nigam, S. Variability of the Great Plains low-level jet: Large-scale circulation context and hydroclimate impacts. *J. Clim.* **2008**, *21*, 1532–1551. [[CrossRef](#)]
33. Branstator, G. Circumglobal teleconnections, the jet stream waveguide, and the North Atlantic Oscillation. *J. Clim.* **2002**, *15*, 1893–1910. [[CrossRef](#)]
34. PaiMazumder, D.; Done, J.M. Potential predictability sources of the 2012 U.S. drought in observations and a regional model ensemble. *J. Geophys. Res. Atmos.* **2016**, *121*, 581–592. [[CrossRef](#)]
35. Malloy, K.M.; Kirtman, B.P. Predictability of Midsummer Great Plains Low-Level Jet and Associated Precipitation. *Weather. Forecast.* **2020**, *35*, 215–235. [[CrossRef](#)]
36. Saha, S.; Moorthi, S.; Wu, X.; Wang, J.; Nadiga, S.; Tripp, P.; Behringer, D.; Hou, Y.-T.; Chuang, H.-Y.; Iredell, M.; et al. The NCEP Climate Forecast System Version 2. *J. Clim.* **2014**, *27*, 2185–2208. [[CrossRef](#)]
37. Shepard, D.S. Computer mapping: The SYMAP interpolation algorithm. In *Spatial Statistics and Models*; Gaile, G.L., Wilmott, C.J., Eds.; Springer-Science +Business Media: Dordrecht, The Netherlands, 1984; pp. 133–145.
38. Daly, C.; Neilson, R.P.; Phillips, D.L. A statistical-topographic model for mapping climatological precipitation over mountainous terrain. *J. Appl. Meteorol. Climatol.* **1994**, *33*, 140–158. [[CrossRef](#)]
39. Chen, M.; Shi, W.; Xie, P.; Silva, V.B.S.; Kousky, V.E.; Higgins, R.W.; Janowiak, J.E. Assessing objective techniques for gauge-based analyses of global daily precipitation. *J. Geophys. Res. Atmos.* **2008**, *113*, 1–13. [[CrossRef](#)]
40. Wilks, D.S. Enforcing calibration in ensemble postprocessing. *Q. J. R. Meteorol. Soc.* **2017**, *144*, 76–84. [[CrossRef](#)]
41. Saha, S.; Moorthi, S.; Pan, H.-L.; Wu, X.; Wang, J.; Nadiga, S.; Tripp, P.; Kistler, R.; Woollen, J.; Behringer, D.; et al. The NCEP Climate Forecast System Reanalysis. *Bull. Am. Meteorol. Soc.* **2010**, *91*, 1015–1058. [[CrossRef](#)]
42. NOAA National Operational Model Archive and Distribution System (NOMADS). Available online: <https://nomads.ncep.noaa.gov> (accessed on 3 December 2023).
43. Weaver, S.J.; Ruiz-Barradas, A.; Nigam, S. Pentad evolution of the 1988 drought and 1993 flood over the Great Plains: An NARR perspective on the atmospheric and terrestrial water balance. *J. Clim.* **2009**, *22*, 5366–5384. [[CrossRef](#)]
44. Wilks, D.S. *Statistical Methods in the Atmospheric Sciences*; Elsevier: Amsterdam, The Netherlands, 2011; 676p.
45. Murakami, M. Large-scale aspects of deep convective activity over the GATE area. *Mon. Weather. Rev.* **1979**, *107*, 994–1013. [[CrossRef](#)]
46. Lees, J.M.; Park, J. Multi-taper spectral analysis: A stand-alone C-subroutine. *Comput. Geosci.* **1995**, *21*, 199–236. [[CrossRef](#)]
47. Livezey, R.E.; Chen, W.Y. Statistical field significance and its determination by Monte Carlo techniques. *Mon. Weather. Rev.* **1983**, *111*, 46–59. [[CrossRef](#)]
48. Jiang, X.; Lau, N.-C.; Held, I.M.; Ploshay, J.J. Mechanisms of Great Plains low-level jet as simulated in an AGCM. *J. Atmos. Sci.* **2007**, *64*, 532–547. [[CrossRef](#)]
49. Barlow, M.; Gutowski, W.J.; Gyakum, J.R.; Katz, R.W.; Lim, Y.-K.; Schumacher, R.S.; Wehner, M.F.; Agel, L.; Bosilovich, M.; Collow, A.; et al. North American extreme precipitation events and related large-scale meteorological patterns: A review of statistical methods, dynamics, modeling, and trends. *Clim. Dyn.* **2019**, *53*, 6835–6875. [[CrossRef](#)]

50. Li, S.; Robertson, A.W. Evaluation of submonthly precipitation forecast skill from global ensemble prediction systems. *Mon. Weather. Rev.* **2015**, *143*, 2871–2889. [CrossRef]
51. Mariotti, A.; Ruti, P.M.; Rixen, M. Progress in subseasonal to seasonal prediction through a joint weather and climate community effort. *Npj Clim. Atmos. Sci.* **2018**, *1*, 4. [CrossRef]
52. Jaimes-Correa, J.C.; Muñoz-Arriola, F.; Bartelt-Hunt, S. Modeling water quantity and quality nonlinearities for watershed adaptability to hydroclimate extremes in agricultural landscapes. *Hydrology* **2022**, *9*, 80. [CrossRef]
53. Sarzaeim, P.; Muñoz-Arriola, F. A Method to Estimate Climate Drivers of Maize Yield Predictability Leveraging Genetic-by-Environment Interactions in the US and Canada. *Agronomy* **2024**, *14*, 733. [CrossRef]
54. Nielsen, R.L. Corn Management for Extreme Conditions. Corny News Network (Purdue University). 2012. Available online: <https://www.agry.purdue.edu/ext/corn/news/timeless/extremecornmgmt.html> (accessed on 10 February 2018).
55. Melton, F.S.; Huntington, J.; Grimm, R.; Herring, J.; Hall, M.; Rollison, D.; Erickson, T.; Allen, R.; Anderson, M.; Fisher, J.B.; et al. OpenET: Filling a critical data gap in water management for the western United States. *JAWRA J. Am. Water Resour. Assoc.* **2022**, *58*, 971–994. [CrossRef]
56. Volk, J.M.; Huntington, J.L.; Melton, F.S.; Allen, R.; Anderson, M.; Fisher, J.B.; Kilic, A.; Ruhoff, A.; Senay, G.B.; Minor, B.; et al. Assessing the accuracy of OpenET satellite-based evapotranspiration data to support water resource and land management applications. *Nat. Water* **2024**, *2*, 193–205. [CrossRef]
57. Wilson, A.; Cifelli, R.; Munoz-Arriola, F.; Giovannettone, J.; Vano, J.; Parzybok, T.; Dufour, A.; Jasperse, J.; Mahoney, K.; McCormick, B. Efforts to Build Infrastructure Resiliency to Future Hydroclimate Extremes. In *Geo-Extreme 2021*; ASCE: Reston, VA, USA, 2021; pp. 222–233. [CrossRef]
58. Dagon, K.; Truesdale, J.; Biard, J.C.; Kunkel, K.E.; Meehl, G.A.; Molina, M.J. Machine Learning, Based Detection of Weather Fronts and Associated Extreme Precipitation in Historical and Future Climates. *J. Geophys. Res. Atmos.* **2022**, *127*, e2022JD037038. [CrossRef]
59. Pandey, V.; Srivastava, P.K.; Mall, R.K.; Munoz-Arriola, F.; Han, D. Multi-Satellite Precipitation Products for Meteorological Drought Assessment and Forecasting in Bundelkhand region of Central India. *Geocarto Int.* **2020**, *37*, 1899–1918. [CrossRef]
60. Rehana, S.; Yeleswarapu, P.; Basha, G.; Munoz-Arriola, F. Precipitation and Temperature Extremes and Association with Large-scale Climate Indices: An Observational Evidence over India. *J. Earth Syst. Sci.* **2022**, *131*, 170. [CrossRef]
61. Carrillo, C.M.; Muñoz-Arriola. Precipitation, Low-Level Jet, and Geopotential Height Data for Analyzing Sources of Predictability in the US Northern Great Plains [Data Set]. *Zenodo*. 2021. Available online: <https://zenodo.org/records/5784508> (accessed on 19 July 2024).

Disclaimer/Publisher’s Note: The statements, opinions and data contained in all publications are solely those of the individual author(s) and contributor(s) and not of MDPI and/or the editor(s). MDPI and/or the editor(s) disclaim responsibility for any injury to people or property resulting from any ideas, methods, instructions or products referred to in the content.